UNIVERSITY of York

This is a repository copy of *Relativistic domain-wall dynamics in van der Waals antiferromagnet MnPS3*.

White Rose Research Online URL for this paper:
https://eprints.whiterose.ac.uk/189038/

Version: Published Version

Article:
Alliati, Ignacio M., Evans, Richard F.L. orcid.org/0000-0002-2378-8203, Novoselov, Kostya S. et al. (1 more author) (2022) Relativistic domain-wall dynamics in van der Waals antiferromagnet MnPS3. npj Computational Materials. 3. ISSN 2057-3960

https://doi.org/10.1038/s41524-021-00683-6

Reuse
This article is distributed under the terms of the Creative Commons Attribution (CC BY) licence. This licence allows you to distribute, remix, tweak, and build upon the work, even commercially, as long as you credit the authors for the original work. More information and the full terms of the licence here: https://creativecommons.org/licenses/

Takedown
If you consider content in White Rose Research Online to be in breach of UK law, please notify us by emailing eprints@whiterose.ac.uk including the URL of the record and the reason for the withdrawal request.

White Rose university consortium
Universities of Leeds, Sheffield & York

eprints@whiterose.ac.uk
https://eprints.whiterose.ac.uk/

npj Computational Materials

www.nature.com/npjcompumats

ARTICLE OPEN

Check for updates

Relativistic domain-wall dynamics in van der Waals antiferromagnet $MnPS_3$

Ignacio M. Alliati[1], Richard F. L. Evans[2], Kostya S. Novoselov[3] and Elton J. G. Santos[4,5]✉

The discovery of two-dimensional (2D) magnetic van der Waals (vdW) materials has flourished an endeavor for fundamental problems as well as potential applications in computing, sensing and storage technologies. Of particular interest are antiferromagnets, which due to their intrinsic exchange coupling show several advantages in relation to ferromagnets such as robustness against external magnetic perturbations. Here we show that, despite of this cornerstone, the magnetic domains of recently discovered 2D vdW $MnPS_3$ antiferromagnet can be controlled via magnetic fields and electric currents. We achieve ultrafast domain-wall dynamics with velocities up to ~3000 m s^{-1} within a relativistic kinematic. Lorentz contraction and emission of spin-waves in the terahertz gap are observed with dependence on the edge termination of the layers. Our results indicate that the implementation of 2D antiferromagnets in real applications can be further controlled through edge engineering which sets functional characteristics for ultrathin device platforms with relativistic features.

npj Computational Materials (2022)8:3 ; https://doi.org/10.1038/s41524-021-00683-6

INTRODUCTION

The emergence of magnetism in 2D vdW materials has opened exciting avenues in the exploration of spin-based applications at the ultimate level of few-atom-thick layers. Remarkable properties including giant tunneling magnetoresistance[1–3] and layer stacking dependent magnetic phase[4,5] have recently been demonstrated. Even though these studies show that rich physical phenomena can be observed in 2D ferromagnets[6–9], the dynamics of domain walls which determine whether such compounds can be effectively implemented in real-life device platforms remains elusive. Very few reports have shed some light on the intriguing behavior of magnetic domains[10,11] and their walls[12] in ferromagnetic layered materials. The scenario is even less clear for 2D antiferromagnets where the antiferromagnetic exchange coupling between spins adds a level of complexity in terms of the manipulation of the magnetic moments by conventional techniques as zero net magnetization is obtained[13]. Indeed, recent measurements using tunneling magnetoresistance, a common approach for ferromagnetic materials, unveiled that antiferromagnetic correlations persist down to the level of individual monolayers of $MnPS_3$[14]. This result suggests that yet unexplored ingredients at low-dimensionality play an important role in the detection and manipulation of the antiferromagnetic order in 2D vdW compounds. Moreover, how domain walls in $MnPS_3$ behave and can be controlled externally in functional devices for practical applications are still open questions.

By using correlated first-principles methods, including Hubbard *U* corrections, large scale Monte Carlo and Landau–Lifshitz–Gilbert equation techniques, we report that electrical currents and, unexpectedly, magnetic fields can move domain walls in monolayer $MnPS_3$ at low-temperatures achieving fast velocities within the km s^{-1} limit. While bulk antiferromagnetic compounds are insensitive to magnetic fields, the interplay between low-dimensionality and edge-type offers control over domain wall dynamics via an initially unthinkable external parameter. In configurations where the layer terminates with either a zigzag array of Mn atoms or dangling bonds, the domain walls are controllable via both currents and magnetic fields at a broad range of magnitudes. For configurations where the edge atoms assume an armchair configuration, the domain wall appears pinned and no motion is observed irrespective of the field intensity or current density applied. Our results indicate a rich variety of possibilities depending on the edge roughness and introduce the layer termination as one of the determinant factors for integration of 2D antiferromagnets in domain-wall-based applications.

RESULTS

Spin dynamics on monolayer $MnPS_3$

We firstly investigate how magnetic domains are formed in monolayer $MnPS_3$ through simulating the zero-field-cooling process for a large square flake of 0.3 μm × 0.3 μm using atomistic spin dynamics which incorporate micro-scale (several Å's) and macro-scale (μm-level) underlying details (see full set of details in Supplementary Notes 1–6). The system is thermally equilibrated above the Curie temperature at 80 K and then linearly cooled to 0 K in a simulated time of 4.0 ns as shown in Fig. 1 and Supplementary Movies S1 and S2. The time evolution of the easy-axis component of the magnetization S_z is used to display the nucleation of the magnetic domains at different temperatures and magnetic fields. While domain walls appeared at zero field with a large extension over the simulation area (Fig. 1a–e), an external field can flush out any domains resulting in a homogeneous magnetization after 2 ns (Fig. 1f–j). We also observed that some simulations at zero field ended up in the formation of a monodomain throughout the surface. This suggests that antiferromagnetic domains may not be intrinsically stable in

[1]School of Mathematics and Physics, Queen's University Belfast, Belfast BT7 1NN, UK. [2]Department of Physics, The University of York, York YO10 5DD, UK. [3]Institute for Functional Intelligent Materials, National University of Singapore, Singapore 117544, Singapore. [4]Institute for Condensed Matter Physics and Complex Systems, School of Physics and Astronomy, The University of Edinburgh, Edinburgh EH9 3FD, UK. [5]Higgs Centre for Theoretical Physics, The University of Edinburgh, Edinburgh EH9 3FD, UK.
✉email: esantos@ed.ac.uk

Published in partnership with the Shanghai Institute of Ceramics of the Chinese Academy of Sciences

npj nature partner journals

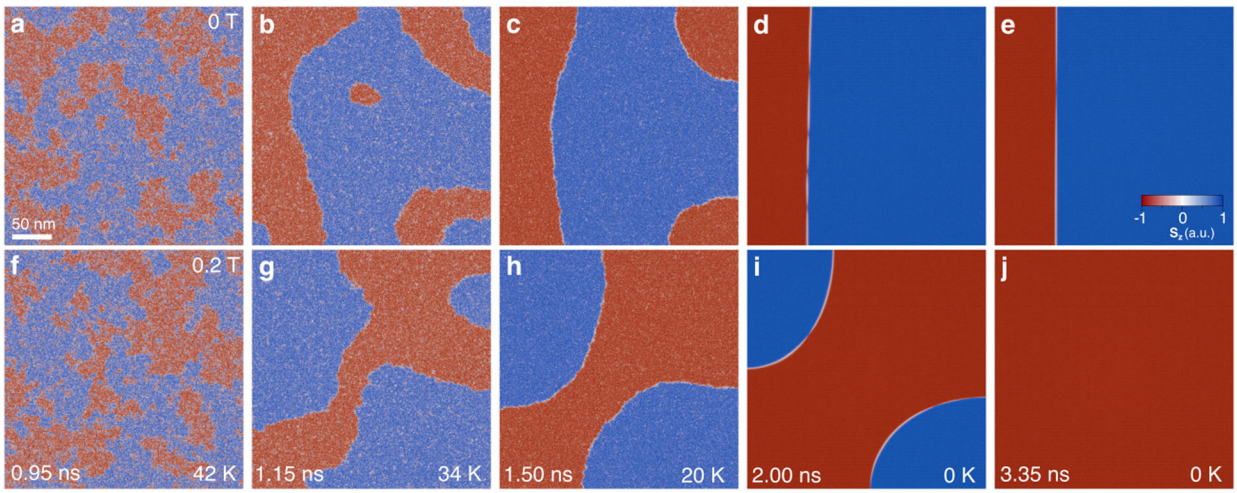

Fig. 1 Magnetic domain evolution of a 2D antiferromagnet. Snapshots of the dynamic spin configuration of monolayer $MnPS_3$ during field-cooling at different temperatures (K), time steps (ns) and different magnetic fields: **a–e** 0 T and **f–j** 0.2 T. The out-of-plane component of the magnetization S_z is used to follow the evolution in a 0.3 μm × 0.3 μm square flake. Labels on temperatures and time are the same for both magnitudes of the field at the same column. Color scale in **e** shows the variation of S_z. To provide a better visualization of the domains we inverted the color scheme for the two sublattices. That is, spin up (spin down) corresponds to red (blue) for one of the sublattices, and blue (red) for the other. This convention results in a single color for a given domain. See Supplementary Note 8 for further details.

$MnPS_3$ similarly as in ferromagnetic layered materials, e.g., CrI_3[12]. The metastability of the domains prevents the wall profiles from reaching a truly ground-state configuration as they initially appear winded at 0 K (Fig. 1d). Undertaking the rendering of the domain wall at different time frames (Supplementary Fig. 10), we noticed that several nodes of a few lattice sites in diameter are created but incidentally evolved to an unwound state (Fig. 1e). A close look reveals a continuous rotation of the spins over the extension of the wall pushing the nodes out of the domain wall profile (Supplementary Movie S3). Such repulsive interactions between nodes can extend as long as ~95 nm along the wall which is more that two order of magnitudes larger than the thickness (0.8 nm[15]) of the monolayer $MnPS_3$. At longer times, the domain wall reaches stability and does not show any sudden variations on the spin configurations.

To determine whether the interplay between metastability and the high magnetic anisotropy of $MnPS_3$ could give additional features to the domain walls, we analyze the local behavior of the spins in the domain wall (Fig. 2). We notice that as the spins rotate from one magnetic domain to another they tend to align with the zig-zag crystallographic direction displaying an angle of $\phi = 64.02^o$ (Fig. 2a, b). The magnitude of ϕ slightly depends on the starting conditions of the simulations having not effect on the domain wall dynamics. The chirality does not systematically vary with magnetic field or temperature, although elevated temperatures lead to more magnetization fluctuations that can increase the appearance of different chiralities. Moreover, 2D magnetic materials seem to exhibit polychiral domain walls of Néel, Bloch and hybrid character as previously demonstrated[12].

The projections of the total magnetization at the wall over the out-of-plane (S_z) and in-plane (S_x, S_y) components show sizeable magnitudes of S_y and S_x as the spins transition from one domain to another despite the easy-axis anisotropy along of S_z (Fig. 2c, d). This indicates a domain wall of hybrid characteristics rather than one of Bloch and Néel type (Fig. 2e, f). We can extract the domain wall width $\sigma_{x,y,z}$ by fitting the different components of the magnetization (S_x, S_y, S_z) to standard equations[16] of the form:

$$S_j = \frac{1}{\cosh(\pi(j - j_0)/\sigma_j)}, \quad \text{with} \quad j = x, y \tag{1}$$

$$S_z = \tanh(\pi(z - z_0)/\sigma_z) \tag{2}$$

where j_0 and z_0 are the domain wall positions at in-plane and out-of-plane coordinates, respectively. The domain wall widths are within the range of $\sigma_{x,y,z} = 3.40$–3.50 nm. Such small widths are commonly observed in permanent magnetic materials[16] due to their exceptionally high magnetic anisotropy such as $Nd_2Fe_{14}B$ (3.9 nm), $SmCo_5$ (2.6 nm), CoPt (4.5 nm) and Mn overlayers on Fe (001) (4.55 nm)[17]. In these systems, magnetic domains are energetically stable after zero-field cooling due to long-range dipole interactions which were also checked in our study resulting in no modifications of the results. Therefore, $MnPS_3$ reunites characteristics from soft-magnets (large area uniform magnetization) and hard-magnets (large magnetic anisotropy, narrow domain walls) within the same material.

Current-driven domain wall dynamics

An outstanding question raised by these hybrid features is whether the domain walls can be manipulated by external excitations such as electrical currents or magnetic fields. It is well known that antiferromagnets are insensitive to magnetic fields but are rather controllable through currents particularly in high-anisotropy materials[13,18]. However, the low dimensionality together with the underlying symmetry of the honeycomb structure may lead to features on the dynamics of domain walls not yet observed in bulk antiferromagnets. To investigate this we simulate the spin-transfer torque (STT) induced by spin-polarized currents and the effect of magnetic fields on a large nano-flake of monolayer $MnPS_3$ of dimensions of 300 nm × 50 nm (see Supplementary Note 9 for details). This setup is similar as those used in magnetic wires used in racetrack platforms[19,20], which allows its rapid implementation on ongoing investigations. Other mechanisms, such as spin-Hall effect (SHE) induced spin-orbit torque (SOT) were not considered. Since the domain wall motion is mainly driven by STT as the local magnetization textures cause a direct change of angular momentum of the incoming spin-polarized current inducing the magnetization to move. For completeness, we include adiabatic and non-adiabatic contributions to the STT (Supplementary Note 9). The domain wall is initially stabilized from one-atom-thick wall which broadens and develops a profile during the thermalization over a simulation time of 0.5 ns. The finite width of the nanowire assists in the formation of the domain walls. The system is then allowed to evolve for longer times (~2 ns)

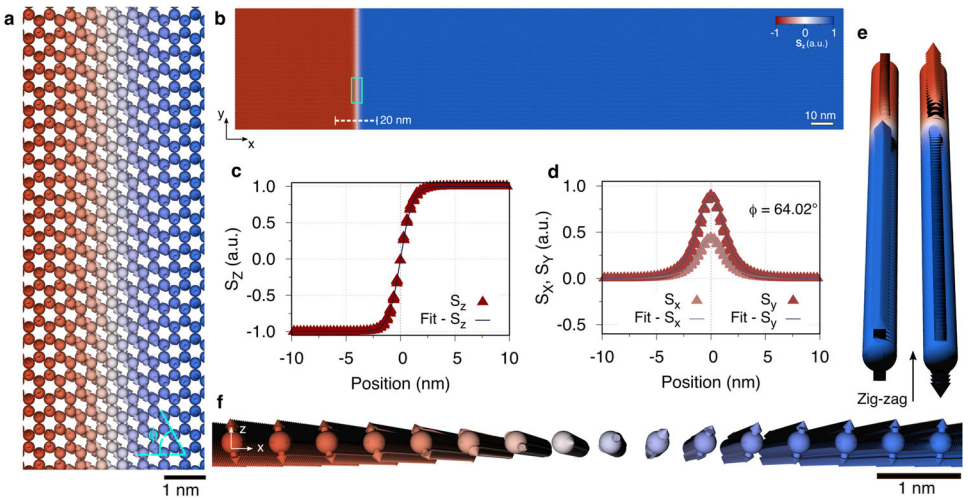

Fig. 2 Hybrid domain wall formation and spin rotation. a, **b** Local and global view, respectively, of a snapshot of one of the spin configurations in a 300 nm × 50 nm ribbon of $MnPS_3$. The small rectangle in **b** corresponds to area studied in **a**. The out-of-plane component of the magnetization S_z(color map) is utilized to monitor the formation of the domain wall. Spins rotated across the wall in pairs forming an angle ϕ with the zig-zag crystallographic direction of the honeycomb lattice of 64.02°. The system is at zero magnetic field and 0 K. **c**, **d** Profile of the magnetization along the domain wall projected along S_z and the in-plane (S_x, S_y) components, respectively. Fitting curves are obtained using Eqs. (1) and (2). We computed domain wall widths $\sigma_z = 3.41$ nm (±0.03) and $\sigma_{x,y} = 3.50$ nm (±0.06). **e**, **f** Top and side views, respectively, of the rotation of the magnetization along the domain wall. Both S_x and S_y show variations along the wall altogether with S_z which indicate a hybrid character of the domain wall, i.e., neither Bloch nor N& eel. Colors follow the scale bar in **b**.

to ensure that no changes are observed in the system close to the end of the dynamics.

Surprisingly, both electric currents and magnetic fields are able to induce the motion of domain walls in the antiferromagnetic $MnPS_3$ resulting in a broad range of velocities (Figs. 3 and 4). For current-induced domain wall motion, wall velocities up to $v = 3000$ m s^{-1} are seen at a maximum current density of $j = 80 \times 10^9$ A cm^{-2} (Fig. 3a, b). At such large values of j, we observe primarily two regimes that are characterized by different dependences of v with j. For $j \leq 30 \times 10^9$ A cm^{-2} (Fig. 3a) a linear dependence is noticed which can be described by a one-dimensional model (Supplementary Note 10) as:

$$v = C_c j \tag{3}$$

where $C_c = \frac{\mu_B \sigma}{2\alpha e m_s t_z}\theta_{SH}$, with μ_b the Bohr magneton, σ the domain wall width, θ_{SH} the spin Hall angle, α the Gilbert damping parameter, e the electron charge, m_s the modulus of the magnetization per lattice, and t_z the layer thickness. Eq. (3) is consistent with adiabatic spin-transfer mechanisms in thin antiferromagnets[13,18,21] where the conduction electrons from the current transfer angular momentum to the spins of the wall which keeps its coherence through a steady motion (Fig. 4a, b and Supplementary Movie S4). The value of $C_c = 67.11 \times 10^{-13} m^3 C^{-1}$ extracted from our simulation data helps to find other parameters not easily accessible in experiments or from theory, e.g., θ_{SH}. The magnitude of θ_{SH} determines the conversion efficiency between charge and spin currents, and it is the figure of merit of any spintronic application. Using the definition of C_c (Supplementary Note 10), we can estimate $\theta_{SH}(\%) = 0.010$ which is comparable to standard heterostructures and metallic interfaces[22] but at a much thinner limit. This suggests $MnPS_3$ as a potential layered compound for power-efficient device platforms. For $j \geq 40 \times 10^9$ A cm^{-2} the wall velocities tend to saturate to a maximum magnitude near 3000 m s^{-1} (Fig. 3a) with a deviation from the linear dependence observed previously (Eq. (3)). This intriguing behavior can be understood in terms of the relativistic kinematics of antiferromagnets[13,23]. As the wall velocities approach the maximum group velocities (v_{g1}, v_{g2}), which sets the maximum speed for spin interactions into the system, relativistic effects in terms of the Lorentz invariance become more predominant. This is due to the finite inertial mass of the antiferromagnetic domain wall which can be decomposed into spin-waves represented through relativistic wave equations[21,23,24]. We can extend this idea further in a 2D vdW antiferromagnet by examining the variations of several quantities via special relativity concepts. For instance, the variation of the wall velocities versus current densities can be well analyzed using:

$$v = C_c j \sqrt{1 - (v/v_{g2})^2} \tag{4}$$

where v_{g2} is the maximum spin-wave group velocity at one of the branches of the magnon dispersion which corresponds to the speed of light in the system[21,24] (Supplementary Note 12). Eq. (4) includes quasi-relativistic corrections[21,24] to the linear dependence recorded at low values of the density (Eq. (3)) and can be solved self-consistently in v for each magnitude of j. Strikingly, Eq. (4) provides an accurate description of the wall velocity not only at low magnitudes of the density, where relativistic effects are rather small, but also for $j \geq 40 \times 10^9$ A cm^{-2}. At such limit, the domain wall width σ and the domain wall mass M_{DW} shrinks and increases, respectively, exhibiting effects similar to the Lorentz contraction (Fig. 3c, d). These phenomena can be reasoned by (see Supplementary Note 10 for details):

$$\sigma = \sigma_o \sqrt{1 - (v/v_{g2})^2} \tag{5}$$

$$M_{DW} = \frac{2\rho w t_z \pi}{\sigma_o \sqrt{1 - (v/v_{g2})^2}} \tag{6}$$

where σ_o is domain wall width at rest (~3.41 nm), which keeps its magnitude at the low-velocity regime, $\rho = \frac{1}{J_{1NN}\gamma^2}$ (with J_{1NN} the exchange parameter for the first nearest-neighbors and γ the gyromagnetic ratio), w is the width of the stripe of the material, and t_z is the layer thickness. The importance of Eqs. (5) and (6) resides on the additional features provided on the internal domain wall structure as well their complementary aspect on the relativistic effects. There is a sound agreement between the simulation data (Fig. 3c, d) and Eqs. (5)–(6) over a wide range of velocities with minor deviations occurring above 2500 m s^{-1} due to non-linear spin excitations. It is worth mentioning that at such

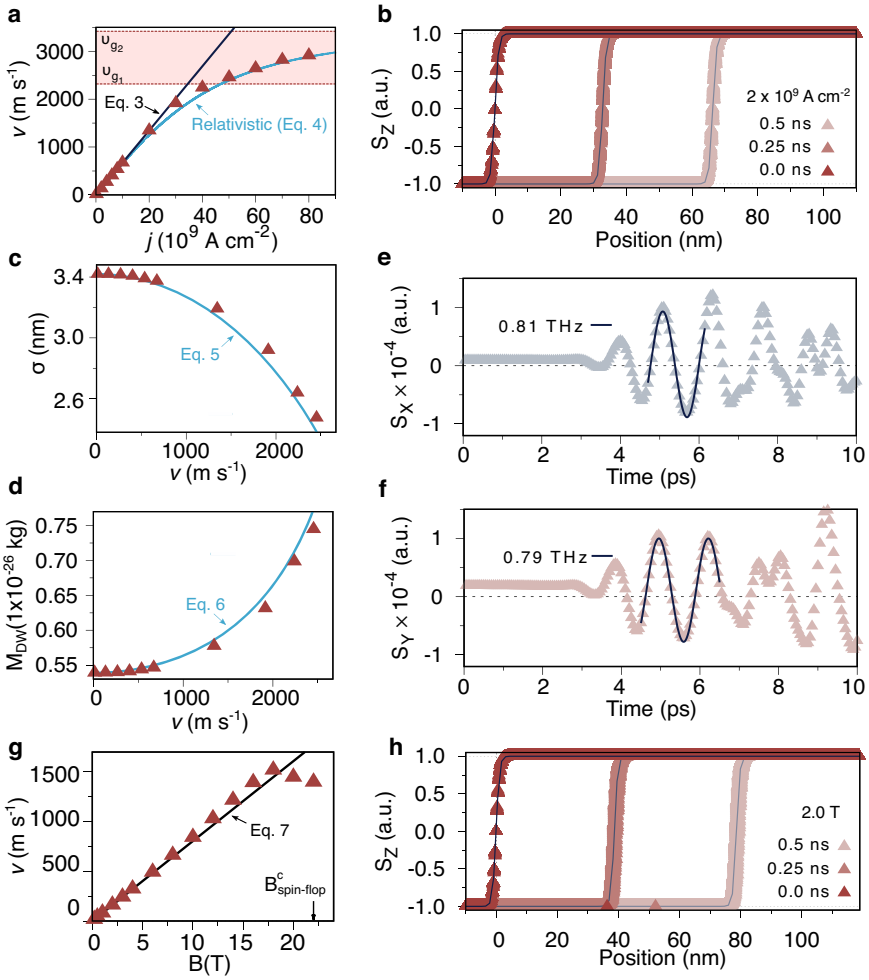

Fig. 3 Relativistic effects on domain wall motion. a Simulated domain wall velocity v (m s^{-1}) versus current density j (10^9 A cm^{-2}) (triangles) considering two fits to the data. In the low-velocity regime, Eq. (3) is used to describe the linear dependence (black curve). In the relativistic regime, Eq. (4) provides an accurate description over the entire range of densities. Maximum group velocities v_{g1} and v_{g2} are shown for comparison via horizontal dashed lines in the colored region. **b** Variation of the out-of-plane component of the magnetization S_z across the domain wall with a current density of 2×10^9 A cm^{-2} at $t = 0.0, 0.25, 0.5$ ns. The calculated points are fitted to Eq. (2) shown with the solid line. The variation in position of the center of the domain wall as a function of time is used to extract the wall velocity which is an average over all atoms at the domain wall. **c**, **d** Current-driven domain wall width σ (nm) and domain wall mass M_{DW}, respectively, versus v. Fits to Eqs. (5) and (6) are included for comparison. **e, f** In-plane components of the magnetization $S_{x,y}$ (a.u.) versus time (ps), respectively, for $j = 2 \times 10^9$ A cm^{-2}. Frequencies within the range of 0.79−0.81 THz can be extracted from $S_{x,y}$ shown via the solid curves in a full circle. **g**, Domain wall velocity versus magnetic field applied perpendicular to the surface. The dashed line is given by $y = 86.28x$ with linear regression coefficient $R^2 = 0.9996$. The critical field for spin-flop transition $B^c_{spin-flop}$ is highlighted. **h** Similar as **b** but at an applied field of 2.0 T. The initial condition shows that the spin directions of all atoms at the same x (and any y) appear superimposed on top of each other, revealing a highly ordered system. As the wall motion starts, atoms at the same x but different y no longer have the same spin direction, leading to a continuous distribution of spins.

large wall velocities, spin waves or magnons are emitted throughout the layer with frequencies in the terahertz regime (Fig. 3e, f). These excitations can be found in the wake of the wall forming simultaneously in front and behind the wall motion (see Supplementary Movie S5). Analyzing the variations of S_z over time at different j (Supplementary Fig. 12), we noticed that high currents generated precession of the spins around the easy-axis with their high in-plane projections (S_x, S_y) being transmitted through spin-waves into the system (Fig. 3e, f). This is critical at large values of j where the variation of the position of the domain wall with time results in two velocities before and after the magnons start being excited (Supplementary Fig. 12). This behavior is particularly turbulent at longer times as the wall profile can not be defined any more with the appearance of several vortex, antivortex and spin textures at both edges of the layer and inside the flake (Supplementary Movie S6).

Spin excitation and magnon propagation

To have a thorough understanding of the characteristics of spin excitations on the domain wall dynamics in $MnPS_3$, we have developed an analytical model using linear spin-wave theory[25,26] that accounts on the magnon dispersion $\varepsilon(\mathbf{k})$ and their group velocities $v_g(\mathbf{k}) = \frac{\partial \varepsilon(\mathbf{k})}{\partial \mathbf{k}}$ over the entire Brillouin zone. Supplementary Note 12 provides a full description of the details involved. The maximum spin-wave group velocities (v_{g1}, v_{g2}) that $MnPS_3$ can sustain at different magnon branches (Supplementary Fig. 13) are in the range from $v_{g1} = 2323$ m s^{-1} to $v_{g2} = 3421$ m s^{-1} (Fig. 3a). These magnitudes correspond to the highest velocities at which spin excitations can propagate into the system accordingly to the amount of energy (Supplementary Fig. 13a) transferred through current or field. Moreover, v_{g1} and v_{g2} correspond to spin waves propagating in opposite direction in the wake of the domain wall

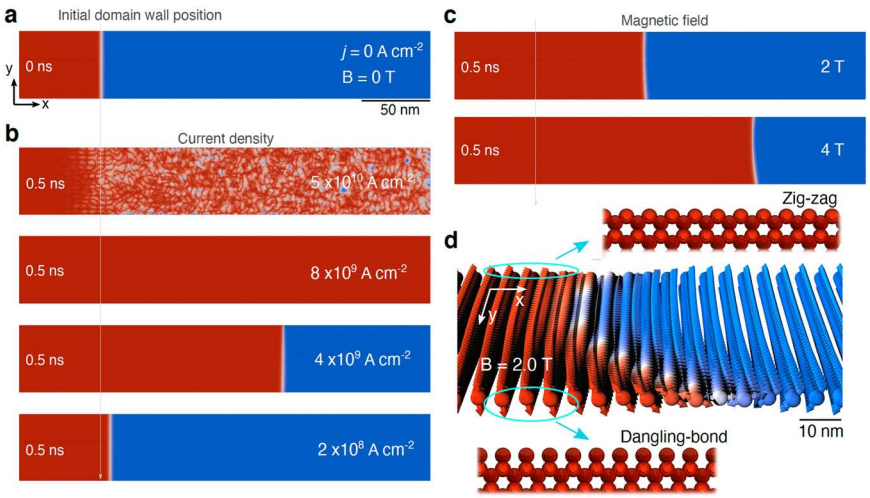

Fig. 4 Field- and current-induced domain wall dynamics in a 2D antiferromagnet. a Snapshot of the initial domain wall configuration ($j = 0$, $B = 0$) used for both current and field after initial equilibration. The initial time is set to $t = 0$ ns on the wall dynamics. A 300 nm × 50 nm flake is considered in all simulations. **b**, **c** Snapshots of the domain wall dynamics in $MnPS_3$ induced by different electrical currents (2×10^8–5×10^{10} A cm^{-2}) and magnetic fields (2 T and 4 T), respectively. The dynamics is shown at the same time evolution of 0.5 ns. Turbulent states are observed for large current densities where domain walls are non-existent. **d** Close look of the snapshot of the field-induced domain wall motion at $B = 4.0$ T in **c**. The presence of different edges (zigzag and dangling-bond) terminating the layer along y induces a bending of the wall profile under the field and consequently a slight asymmetry in the displacement of the wall. Only Mn atoms in the honeycomb lattice are shown.

as they follow the symmetry of the magnon dispersion over the Brillouin zone (Supplementary Fig. 13b, c). It is worth mentioning that recent mechanisms in terms of magnon pair emission[27] cannot be rule out given the pure relativistic origin of the magnon generation, combination and annihilation. Indeed, there is a good agreement with the numerically calculated wall-velocities where the spin-waves start being emitted into the sheet (~2248 m s^{-1}), and the wall saturates to its maximum speed (~2970 m s^{-1}). The slightly lower values obtained in the simulations relative to v_{g1} and v_{g2} are due to the effect of damping on the propagation of domain walls due to the emission of spin-waves. A similar feature has been observed in the past in 3D ferromagnetic[28,29] and antiferromagnetic[21,30] compounds but the emergence of such phenomena in a 2D vdW antiferromagnet is unforeseen. Additionally, we can estimate a maximum wave frequency ($f_{max} = \hbar\varepsilon/2\pi$) corresponding to v_{g2} of about 4.03 THz. This value surpasses those measured in the state-of-the-art antiferromagnetic materials such as in MnO[31], NiO[32,33], $DyFeO_3$[34], $HoFeO_3$[35] and heterostructures combining MnF_2 and platinum[36] by several times. This implies that antiferromagnetic domain walls in $MnPS_3$ can be used as a terahertz source of electric signal at the ultimate limit of a few atoms thick layer.

Field-driven domain wall dynamics

Remarkably, the application of a magnetic field results in a very counter-intuitive behavior as the domain wall moves with velocities as high as ~1500 m s^{-1} (Fig. 3g, h and Supplementary Note 13 for additional discussions). We can fit most of the field-induced domain wall dynamics for $B \leq 20$ T with:

$$v = 86.28\,B \tag{7}$$

with a linear regression coefficient of $R^2 = 0.9996$. The motion is steady, keeping the wall shape throughout the motion. We observe however that both the domain wall width and the domain wall mass change their magnitudes in opposite trend as that observed in the current-driven domain wall dynamics (Supplementary Fig. 15). We attribute this difference to the distinct operation of the external stimulus on the domain wall. In the current-driven case, the action is tightly focused at the center of the wall, where the angular change in neighboring spins is the largest. For large currents the wall is not able to fully relax its spin profile leading to a contraction in the wall width as observed in the atomistic simulations. From a more theoretical standpoint, however, the domain-wall contraction is a relativistic effect due to the invariance of the antiferromagnetic Lagrangian[21,24,27]. Both views are complementary and provide a thorough explanation of the high-speed phenomena observed on $MnPS_3$.

In contrast, the magnetic field acts across the whole wall and tends to strengthen the spin flop (SF) state, which in turn leads to an increase in the domain wall width with increasing field strength (Supplementary Fig. 15a). This effect compensates any relativistic effects that might be present during the field-driven domain wall (Supplementary Fig. 15b). Wider domain walls naturally have lower mass as they are easier to move until SF states are achieved for fields above 22 T. In addition, some curvature is formed as the wall moves with its starting points from the terminations of the sheet parallel to the wall movement (Fig. 4c and Supplementary Movie 7). The spins around one edge move in advance relative to those at the middle of the system and at the opposite edge creating a curved wall during the motion (see detailed features in Supplementary Movie 8). The domain wall width however suffers negligible modification within this profile (~0.4%) once the curvature is generated. Such deviation from the planar wall shape has been reported in hetero-interfaces formed by NiFe/FeMn bilayers[37] but not yet in a monolayer of a 2D vdW antiferromagnet. This indicates a direct relation between domain-wall motion and the material geometry via edge roughness similarly as in magnetic wires[38]. A close look unveils that the type of edge plays a pivotal role in the domain wall dynamics induced by both magnetic fields and electric currents. Sheets terminated with edge atoms in zig-zag (ZZ) and dangling-bond (DB) configurations (Fig. 4d) in any combination (e.g., ZZ-ZZ, ZZ-DB, DB-DB) can have their domain walls manipulated by currents. Nevertheless, only domain wall in layers with dissimilar edges (e.g., ZZ-DB) can be controlled by magnetic fields. Borders formed by atoms in the armchair (ARM) configuration remain inert irrespective of the stimulus applied (Supplementary Fig. 16). An overall summary is shown in Table 1 with all considered possibilities for edges and driving

forces. Intriguingly, ARM edges under applied currents show a short displacement of the domain wall at earlier stages of the dynamics (~0.07 ns) but rapidly stabilizes to a constant position at longer times. As the current flows through the wall, the spins feel the torque induced by the spin-polarized electrons but rather than reorient the spins to follow the current direction, the spins at the wall precess around the easy-axis with no motion of the domain-wall. This mechanism is shown in details in Supplementary Movies S9 and S10. The ARM edge in this case works as an effective pinning barrier for domain-wall propagation. We also noticed that there is no spin-wave emission as the domain is pined at the edges. The fluctuations of the S_x and S_y projections outside the wall are negligible in magnitude (~10^{-10} a.u.) which are more numerical than physical. Moreover, these negligible oscillations were random and not collective (not coordinated among different atoms). Only when the DW moves throughout the system, the emission of spin waves occurred as showed before.

Edge-mediated domain wall dynamics under magnetic fields

The control of the domain-wall motion in an antiferromagnetic material via magnetic fields creates a playground in the investigation of the role of edges on 2D magnetic materials. The fundamental ingredient that enables such phenomena is based on the underlying magnetic sublattices (e.g., A or B) composing the honeycomb structure (Fig. 5a–c). Despite the border considered, for edge atoms residing at different sublattices the magnetic field induces a torque at each sublattice that mutually compensates each other generating no net displacement of the domain-wall (Supplementary Movie S11). For edge atoms at the same sublattice the effect is additive inducing the translation of the wall. Indeed, we can further confirm this mechanism analyzing the spin interactions present in the system on a basis of a generalized XXZ Heisenberg Hamiltonian in the form of:

$$\mathscr{H} = -\sum_{\langle i,j\rangle} J_{ij}\mathbf{S}_i \cdot \mathbf{S}_j - \sum_{\langle i,j\rangle} \lambda_{ij} S_i^z S_j^z - D\sum_i \left(S_i^z\right)^2 - \mu_s \sum_i \mathbf{S}_i \cdot \mathbf{B}_i \quad (8)$$

where $J_{i,j}$ is the bilinear exchange interactions between spins $\mathbf{S}_i$ and $\mathbf{S}_j$ at sites i and j, λ_{ij} is the anisotropic exchange, D is the on-site magnetic anisotropy and $\mathbf{B}_i$ is the external magnetic field applied along the easy-axis (e.g., B_z). We only include bilinear exchange terms in Eq. (8) since biquadratic exchange interactions are negligible in $MnPS_3$[39]. We considered pair-wise interactions in $\langle i,j\rangle$ up to the third nearest neighbors (3*NN*) (Supplementary Table 1). All parameters are calculated using strongly correlated density functional theory based on Hubbard-*U* methods. Supplementary Notes 1–4 convey the full details of the approaches employed. Eq. (8) is then applied to calculate the spin interactions into the system taking into account any angular variations θ of the spins induced by the field. We determine the stability of the system before and after the application of B_z distinguishing the atoms away from the domain wall from those at the wall (Fig. 6a). Such procedure is instrumental to unveil the influence of the edges on the energetics of the domain-wall dynamics as the atoms at these two spatial regions may respond differently to a magnetic perturbation. In fact, we found that spins that are distanced from the domain-wall (i.e., spin-up for $\theta = 0$, and spin-down for $\theta = 180°$) do not suffer any angular variation with B_z as the layer reached an additional ground-state. Nevertheless, for spins at the domain-wall the ground-state under a finite field ($B_z \neq 0$) is obtained at a value of θ different to that at $B_z = 0$ (Fig. 6b, c). This indicates that the wall spins tend to rotate under magnetic fields and the effect is particularly strong for atoms at the edges. The variations in energy $-\Delta E$ show that when the two edges are similar (Fig. 6b) two different sublattices will be localized at the borders which will respond likewise generating similar variation of energies. As the atoms at the edges are more uncoordinated relative to those in the bulk of the system, they gain more energy from aligning with B_z which allows the spins to rotate more freely but in opposite direction compensating any displacement of the domain-wall. The scenario is completely different when the atoms at the edges belong to the same sublattice such as in a ZZ-DB layer (Fig. 6c). In this case, $-\Delta E$ has a larger variation at the DB edge due to the lesser coordination with neighboring atoms and consequently less exchange energy. This results in a more prompt rotation of the spins at the DB edge than that at the ZZ edge dragging the wall slightly ahead with the field (Supplementary Movie S8). Even though our analysis has been applied for $MnPS_3$ it should be universal for any antiferromagnetic layered material with a honeycomb lattice.

Table 1. Summary of the possible combinations of edges (zigzag (ZZ), armchair (ARM) and dangling bond (DB)) terminating a monolayer $MnPS_3$ that may induce (Y) or not (N) the domain wall motion under current (spin-transfer torque (STT)) or magnetic field.

	ZZ-ZZ	ZZ-DB	DB-DB	ARM-ARM
STT motion	Y	Y	Y	N
Field-driven motion	N	Y	N	N

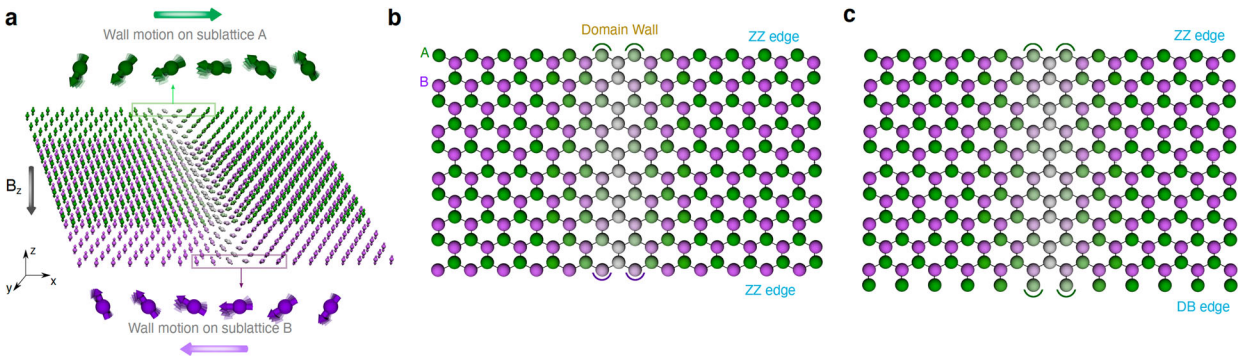

Fig. 5 Edge-induced domain wall dynamics in a 2D antiferromagnet under magnetic fields. a Schematic of the intended wall motion taking place in opposite directions at different sublattices (i.e., A or B) under an external field B_z. Only atoms at one sublattice (green or violet) are shown around each edge to facilitate the view. The rotation of the spins over time at sublattices A (green) and B (violet) are represented with the arrows changing systematically in the background. Only Mn atoms are shown. **b**, **c** Monolayer $MnPS_3$ terminated with both edges in zig-zag (ZZ) configuration, and with a combination of ZZ and dangling-bond (DB) arrangements, respectively. The domain wall is shown at the faint atoms in the middle of the layer.

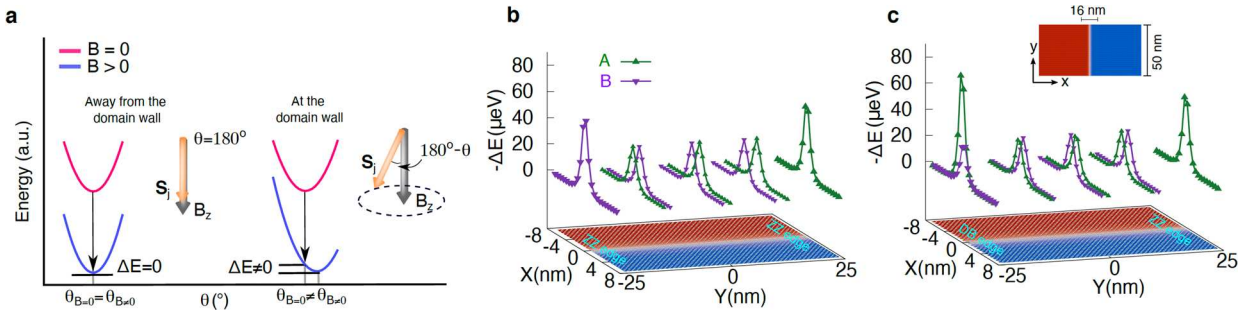

Fig. 6 Sublattice energetics. a Diagram of the energy versus the angle θ defined relative to the z-axis. Away from the domain wall, θ can be either 0° or 180° depending on what sublattice is considered. At the wall, θ can range within 0–180° for one sublattice, and 180–0° for the other. B_z points along of $z < 0$. Spins at the wall ($0° < \theta < 180°$, which excludes fully spin-up and spin-down states) react differently than those away from the wall (i.e., $\theta = 0$ for spin-up or *theta* = 180° for spin down) to an external magnetic field. Only for those at the wall, a finite B_z changes the energetic stability of the system inducing a rotation of the spins as the magnitude of θ changes to an additional energy minimum (e.g., $\theta_{B_z=0} \neq \theta_{B_z \neq 0}$). ΔE shows the energy gained through a rotation to the additional minimum once the field is applied. For the spins away from the wall, B_z causes a rigid shift of the energy curve while preserving its shape. This results in no change in the value of θ for the minimum energy, and thus, no rotation induced locally by the magnetic field. The energy is calculated via Eq. (8). **b**, **c** Plots of $-\Delta E$ for few atoms at different regions of the layer such as at the edges, near the edges and middle of the sheet for systems with ZZ-ZZ and ZZ-DB edges, respectively. The different sublattices (A and B) are shown individually in different colored curves. We plot $-\Delta E$ instead of ΔE to better display the variations of energy at different parts of the system. The inset in **f** shows a side view of the layer with the dimensions considered in the model.

DISCUSSION

One of the implications for having uncompensated spins at the edges selectively controlling domain-wall motion in 2D vdW antiferromagnets is that depending how the layer is oriented in a device-platform we can have many possibilities to induce domain wall dynamics. By engineering the type of edges in $MnPS_3$ we can either induce a fast domain-wall dynamics through both current and magnetic fields, or no motion whatsoever via geometrical constrictions. Our findings also indicate that 2D layered antiferromagnets would not be invisible to common magnetic probes. Indeed, the recent experimental demonstration of field-dependent tunneling magneto resistance observed in $MnPS_3$[14] is a substantial evidence that a net magnetization is present into the system, which following our findings is due to edges. Such characteristic could be critical to generate localized magnetic moments that would allow further control of magnetic processes involving interfaces and heterostructures. In this case the antiferromagnetic layer can play a more active role in magnetic structures rather than induce exchange bias in an adjacent ferromagnetic layer[13]. We foreseen that compounds that would have edges with similar sub-lattices would develop a response to a magnetic field despite their atomic composition.

On the experimental realization of our theoretical results, several approaches may be borrowed from those already established and successfully applied to control and characterize edges in other 2D materials, such as in graphene[40,41] and transition metal dichalcogenides[42,43]. The recent demonstration of etching process along certain crystallographic axes allows to obtain atomically sharp edges and exclusively of one type[42]. This opens the prospects of developments of such method in 2D vdW magnets taking into account the stability, degradation and the magnetic properties of the systems. For practical implementations, metallic substrates (e.g., Pt, Ta, W) can be used to induce spin-transfer torque on $MnPS_3$ as recently demonstrated for insulating oxide layers[44]. Indeed, the range of domain-wall velocities predicted in our simulations at low densities (e.g., ~100 m s^{-1} at ~10^8 A cm^{-2}) and fields of <0.8 T can be achieved at similar setup[44] (Supplementary Fig. 18). Such speeds are sufficient to operate domain-wall technologies (e.g., racetracks) at clock rates competitive with existing materials in similar current densities, i.e., permalloy nanowires[19,20]. The field-driven domain wall velocities calculated are also at the same magnitude as those found in magnetic semiconducting thin films, e.g., (Ga,Mn)(As,P) (4–24 m s^{-1} within 25–125 mT)[45,46] and TbFe (~4.72 m s^{-1} at 382 mT) films[45]. The insulating character of $MnPS_3$ may also not be considered as an disadvantage relative to metallic thin films where low heating dissipation and low power consumption can be explored as recently demonstrated for magnetic insulators[44,47]. In addition, the low domain wall mass within $0.55–0.75 \times 10^{-26}$ kg and the narrow domain wall width in 3.4–2.5 nm suggest fast logic on memory devices. The former is at least 4 order of magnitude smaller than those observed on standard magnetic compounds with much larger width[48]. This indicates that massless domain walls may be achieved on 2D magnets where transient effects induced by current pulses can be negligible[49]. This calls for further investigations using the methods developed in our study on different families of 2D vdW magnetic materials. With the rapid integration of magnetic layered materials into device-related applications and the discovery of more compounds with similar characteristics, our predictions set a horizon of possibilities on the investigations of domain wall-mediated 2D antiferromagnetic spintronics.

METHODS

Hubbard-corrected ab initio simulations

Ab-initio calculations were performed using Density Functional Theory (DFT) as implemented in the VASP package[50,51]. Within the generalized gradient approximation (GGA), the Perdew–Burke–Ernzerhof (PBE) exchange-correlation functional was used. No van der Waals interactions were taken into account given that the system of interest is a monolayer. A Hubbard U correction was included through the Dudarev formulation[52]. The exchange parameter J was fixed as $J = 0.9$ eV while the U energy was calculated through the linear response method resulting in a magnitude of $U = 2.58$ eV[53–56]. These values of J and U were used in all calculations. Additional details on the DFT calculations, parametrization of the spin Hamiltonian used in the simulations are included in Supplementary Notes 1–4.

Large scale spin dynamics

Macromagnetic quantities such as magnetization, susceptibility or Néel temperature were calculated by atomistic methods previously implemented as described in refs. [12,39] A 50 nm × 50 nm square flake (15580 sites in total) with periodic boundary conditions was utilized for these simulations. Additional details are included in Supplementary Notes 5 and 6.

DATA AVAILABILITY

The data that support the findings of this study are available within the paper and its Supplementary Information.

Received: 22 June 2021; Accepted: 28 November 2021;
Published online: 13 January 2022

REFERENCES

1. Song, T. et al. Giant tunneling magnetoresistance in spin-filter van der waals heterostructures. *Science* **360**, 1214–1218 (2018).
2. Wang, Z. et al. Very large tunneling magnetoresistance in layered magnetic semiconductor CrI3. *Nat. Commun.* **9**, 2516 (2018).
3. Klein, D. R. et al. Probing magnetism in 2d van der waals crystalline insulators via electron tunneling. *Science* **360**, 1218–1222 (2018).
4. Song, T. et al. Switching 2d magnetic states via pressure tuning of layer stacking. *Nat. Mater.* **18**, 1298–1302 (2019).
5. Chen, W. et al. Direct observation of van der waals stacking–dependent interlayer magnetism. *Science* **366**, 983–987 (2019).
6. Guguchia, Z. et al. Magnetism in semiconducting molybdenum dichalcogenides. *Sci. Adv.* **4**, eaat3672 (2018).
7. Macy, J. et al. Magnetic field-induced non-trivial electronic topology in fe3xgete2. *Appl. Phys. Rev.* **8**, 041401 (2021).
8. Meseguer-Sánchez, J. et al. Coexistence of structural and magnetic phases in van der waals magnet cri3. *Nat. Commun.* **12**, 6265 (2021).
9. Chen, L. et al. Magnetic field effect on topological spin excitations in cri_3. *Phys. Rev. X* **11**, 031047 (2021).
10. Thiel, L. et al. Probing magnetism in 2d materials at the nanoscale with single-spin microscopy. *Science* **364**, 973–976 (2019).
11. Zhong, D. et al. Layer-resolved magnetic proximity effect in van der waals heterostructures. *Nat. Nanotechnol.* **15**, 187–191 (2020).
12. Wahab, D. A. et al. Quantum rescaling, domain metastability, and hybrid domain-walls in 2d cri3 magnets. *Adv. Mater.* **33**, 2004138 (2021).
13. Baltz, V. et al. Antiferromagnetic spintronics. *Rev. Mod. Phys.* **90**, 015005 (2018).
14. Long, G. et al. Persistence of magnetism in atomically thin mnps3 crystals. *Nano Lett.* **20**, 2452–2459 (2020).
15. Long, G. et al. Isolation and characterization of few-layer manganese thiophosphite. *ACS Nano* **11**, 11330–11336 (2017).
16. Hubert, A. & Schafer, R. *Magnetic domains: the analysis of magnetic microstructures* (Springer Science and Business Media, 2008).
17. Schlickum, U., Janke-Gilman, N., Wulfhekel, W. & Kirschner, J. Step-induced frustration of antiferromagnetic order in mn on fe(001). *Phys. Rev. Lett.* **92**, 107203 (2004).
18. Jungwirth, T., Marti, X., Wadley, P. & Wunderlich, J. Antiferromagnetic spintronics. *Nat. Nanotechnol.* **11**, 231–241 (2016).
19. Hayashi, M. et al. Current driven domain wall velocities exceeding the spin angular momentum transfer rate in permalloy nanowires. *Phys. Rev. Lett.* **98**, 037204 (2007).
20. Parkin, S. S. P., Hayashi, M. & Thomas, L. Magnetic domain-wall racetrack memory. *Science* **320**, 190–194 (2008).
21. Shiino, T. et al. Antiferromagnetic domain wall motion driven by spin-orbit torques. *Phys. Rev. Lett.* **117**, 087203 (2016).
22. Rojas-Sánchez, J.-C. et al. Spin pumping and inverse spin hall effect in platinum: the essential role of spin-memory loss at metallic interfaces. *Phys. Rev. Lett.* **112**, 106602 (2014).
23. Haldane, F. D. M. Nonlinear field theory of large-spin heisenberg antiferromagnets: semiclassically quantized solitons of the one-dimensional easy-axis néel state. *Phys. Rev. Lett.* **50**, 1153–1156 (1983).
24. Kim, S. K., Tserkovnyak, Y. & Tchernyshyov, O. Propulsion of a domain wall in an antiferromagnet by magnons. *Phys. Rev. B* **90**, 104406 (2014).
25. Oguchi, T. Theory of spin-wave interactions in ferro- and antiferromagnetism. *Phys. Rev.* **117**, 117–123 (1960).
26. Kubo, R. The spin-wave theory of antiferromagnetics. *Phys. Rev.* **87**, 568–580 (1952).
27. Tatara, G., Akosa, C. A. & Otxoa de Zuazola, R. M. Magnon pair emission from a relativistic domain wall in antiferromagnets. *Phys. Rev. Res.* **2**, 043226 (2020).
28. Wieser, R., Vedmedenko, E. Y. & Wiesendanger, R. Domain wall motion damped by the emission of spin waves. *Phys. Rev. B* **81**, 024405 (2010).
29. Bouzidi, D. & Suhl, H. Motion of a bloch domain wall. *Phys. Rev. Lett.* **65**, 2587–2590 (1990).
30. Tveten, E. G., Qaiumzadeh, A. & Brataas, A. Antiferromagnetic domain wall motion induced by spin waves. *Phys. Rev. Lett.* **112**, 147204 (2014).
31. Nishitani, J., Nagashima, T. & Hangyo, M. Terahertz radiation from antiferromagnetic mno excited by optical laser pulses. *Appl. Phys. Lett.* **103**, 081907 (2013).
32. Kampfrath, T. et al. Coherent terahertz control of antiferromagnetic spin waves. *Nat. Photonics* **5**, 31–34 (2011).
33. Satoh, T. et al. Spin oscillations in antiferromagnetic nio triggered by circularly polarized light. *Phys. Rev. Lett.* **105**, 077402 (2010).
34. Kimel, A. V. et al. Ultrafast non-thermal control of magnetization by instantaneous photomagnetic pulses. *Nature* **435**, 655–657 (2005).
35. Mukai, Y., Hirori, H., Yamamoto, T., Kageyama, H. & Tanaka, K. Antiferromagnetic resonance excitation by terahertz magnetic field resonantly enhanced with split ring resonator. *Appl. Phys. Lett.* **105**, 022410 (2014).
36. Vaidya, P. et al. Subterahertz spin pumping from an insulating antiferromagnet. *Science* **368**, 160 (2020).
37. Nikitenko, V. I. et al. Asymmetry in elementary events of magnetization reversal in a ferromagnetic/antiferromagnetic bilayer. *Phys. Rev. Lett.* **84**, 765–768 (2000).
38. Nakatani, Y., Thiaville, A. & Miltat, J. Faster magnetic walls in rough wires. *Nat. Mater.* **2**, 521–523 (2003).
39. Kartsev, A., Augustin, M., Evans, R. F. L., Novoselov, K. S. & Santos, E. J. G. Biquadratic exchange interactions in two-dimensional magnets. *npj Comput. Mater.* **6**, 150 (2020).
40. Baringhaus, J. et al. Exceptional ballistic transport in epitaxial graphene nanoribbons. *Nature* **506**, 349–354 (2014).
41. Murdock, A. T. et al. Controlling the orientation, edge geometry, and thickness of chemical vapor deposition graphene. *ACS Nano* **7**, 1351–1359 (2013).
42. Munkhbat, B. et al. Transition metal dichalcogenide metamaterials with atomic precision. *Nat. Commun.* **11**, 4604 (2020).
43. Lv, R. et al. Transition metal dichalcogenides and beyond: synthesis, properties, and applications of single- and few-layer nanosheets. *Acc. Chem. Res.* **48**, 56–64 (2015).
44. Vélez, S. et al. High-speed domain wall racetracks in a magnetic insulator. *Nat. Commun.* **10**, 4750 (2019).
45. Jeudy, V. et al. Universal pinning energy barrier for driven domain walls in thin ferromagnetic films. *Phys. Rev. Lett.* **117**, 057201 (2016).
46. Thevenard, L. et al. Domain wall propagation in ferromagnetic semiconductors: beyond the one-dimensional model. *Phys. Rev. B* **83**, 245211 (2011).
47. Caretta, L. et al. Relativistic kinematics of a magnetic soliton. *Science* **370**, 1438–1442 (2020).
48. Saitoh, E., Miyajima, H., Yamaoka, T. & Tatara, G. Current-induced resonance and mass determination of a single magnetic domain wall. *Nature* **432**, 203–206 (2004).
49. Vogel, J. et al. Direct observation of massless domain wall dynamics in nanostripes with perpendicular magnetic anisotropy. *Phys. Rev. Lett.* **108**, 247202 (2012).
50. Kresse, G. & Furthmüller, J. Efficient iterative schemes for ab initio total-energy calculations using a plane-wave basis set. *Phys. Rev. B* **54**, 11169 (1996).
51. Kresse, G. & Joubert, D. From ultrasoft pseudopotentials to the projector augmented-wave method. *Phys. Rev. B* **59**, 1758–1775 (1999).
52. Dudarev, S. L., Botton, G. A., Savrasov, S. Y., Humphreys, C. J. & Sutton, A. P. Electron-energy-loss spectra and the structural stability of nickel oxide: An lsda +u study. *Phys. Rev. B* **57**, 1505–1509 (1998).
53. Tian, T. et al. Electronic polarizability as the fundamental variable in the dielectric properties of two-dimensional materials. *Nano Lett.* **20**, 841–851 (2020).
54. Li, L. H., Tian, T., Cai, Q., Shih, C.-J. & Santos, E. J. G. Asymmetric electric field screening in van der waals heterostructures. *Nat. Commun.* **9**, 1271 (2018).
55. Santos, E. J. G. Carrier-mediated magnetoelectric coupling in functionalized graphene. *ACS Nano* **7**, 9927–9932 (2013).
56. Hong, J. et al. Intrinsic controllable magnetism of graphene grown on fe. *J. Phys. Chem. C.* **123**, 26870–26876 (2019).

ACKNOWLEDGEMENTS

R.F.L.E. gratefully acknowledges the financial support of ARCHER UK National Supercomputing Service via the embedded CSE programme (ecse1307). K.S.N. thanks the Ministry of Education (Singapore) through the Research Center of Excellence program (grant EDUN C-33-18-279-V12, I-FIM) for funding support. E.J.G.S. acknowledges computational resources through CIRRUS Tier-2 HPC Service (ec131 Cirrus Project) at EPCC funded by the University of Edinburgh and EPSRC (EP/P020267/1); ARCHER UK National Supercomputing Service (http://www.archer.ac.uk) via Project d429. E.J.G.S. acknowledges the EPSRC Early Career Fellowship (EP/T021578/1) and the University of Edinburgh for funding support.

AUTHOR CONTRIBUTIONS

E.J.G.S. conceived the idea and supervised the project. I.M.A. performed ab initio and Monte Carlo simulations under the supervision of E.J.G.S. I.M.A. and E.J.G.S. elaborated

the analysis and figures. R.F.L.E. implemented the spin-transfer-torque method. E.J.G. S. wrote the paper with inputs from all authors. K.S.N. helped in the analysis and discussions. All authors contributed to this work, read the manuscript, discussed the results, and agreed to the contents of the manuscript.

COMPETING INTERESTS

The authors declare no competing interests.

ADDITIONAL INFORMATION

Supplementary information The online version contains supplementary material available at https://doi.org/10.1038/s41524-021-00683-6.

Correspondence and requests for materials should be addressed to Elton J. G. Santos.

Reprints and permission information is available at http://www.nature.com/reprints

Publisher's note Springer Nature remains neutral with regard to jurisdictional claims in published maps and institutional affiliations.

Open Access This article is licensed under a Creative Commons Attribution 4.0 International License, which permits use, sharing, adaptation, distribution and reproduction in any medium or format, as long as you give appropriate credit to the original author(s) and the source, provide a link to the Creative Commons license, and indicate if changes were made. The images or other third party material in this article are included in the article's Creative Commons license, unless indicated otherwise in a credit line to the material. If material is not included in the article's Creative Commons license and your intended use is not permitted by statutory regulation or exceeds the permitted use, you will need to obtain permission directly from the copyright holder. To view a copy of this license, visit http://creativecommons.org/licenses/by/4.0/.

© The Author(s) 2022